



In-situ synthesis of 3D graphene-polyimide composite

Y. He^a, C. Wang^b, Y. Li^{c,*}, L. He^d, H. Wang^e, C. Wang^f, W. Wang^g, K. Wang^h, Y. Li^a, L. He^a, G. Wang^g, T. Peng^g

^a Gemmological Institute, China University of Geosciences, Wuhan 430074, PR China
^b Hubei Gem and Jewelry Engineering Technology Research Center, Wuhan 430074, PR China
^c School of Materials Science and Engineering, Huazhong University of Science and Technology, Wuhan 430074, PR China
^d Mechanical Engineering, University of Birmingham, Birmingham B15 2TT, UK
^e School of Electrical and Electronic Engineering, Huazhong University of Science and Technology, Wuhan 430074, PR China
^f WMG, Materials Engineering Centre, University of Warwick, CV4 7AL Coventry, UK



ARTICLE INFO

Keywords:

3D graphene
Polyimide
In-situ synthesis
Composite

ABSTRACT

3D graphene-polyimide (3DGP) composites were synthesized via an in-situ synthesis method using 3D graphene (3DG) and polyimide (PI) as raw materials. The synthesis process was controlled by the concentration of PI and the reaction time. The 3DGP composites were characterized by scanning electron microscopy (SEM), transmission electron microscopy (TEM), Fourier transform infrared spectroscopy (FTIR), and thermogravimetric analysis (TGA). The results show that the 3DGP composites have a porous structure and high thermal stability. The tensile strength and elongation at break of the 3DGP composites are 47.8 MPa and 2.7%, respectively, which are significantly higher than those of PI. The 3DGP composites also show excellent electrical conductivity, with a volume resistivity of 32.3 Ω·cm and a surface resistivity of 2–18 Ω·cm. The 3DGP composites are suitable for applications in electronic devices and sensors.

1. Introduction

Graphene, a single layer of carbon atoms arranged in a hexagonal lattice, has attracted significant attention due to its exceptional properties, such as high electrical conductivity, high thermal conductivity, and high mechanical strength. However, graphene is a 2D material, and its application in 3D structures is limited. To overcome this limitation, 3D graphene (3DG) has been developed. 3DG is a 3D porous structure made of interconnected graphene sheets. It has a high surface area and high porosity, which makes it suitable for applications in catalysis, energy storage, and sensors. In this paper, we report the in-situ synthesis of 3DGP composites. The 3DG was synthesized by a chemical method, and the PI was synthesized by a polymerization reaction. The 3DG and PI were then mixed and heated to form the 3DGP composite. The 3DGP composite has a porous structure and high thermal stability. The tensile strength and elongation at break of the 3DGP composite are 47.8 MPa and 2.7%, respectively, which are significantly higher than those of PI. The 3DGP composite also shows excellent electrical conductivity, with a volume resistivity of 32.3 Ω·cm and a surface resistivity of 2–18 Ω·cm. The 3DGP composite is suitable for applications in electronic devices and sensors.

(2DG), which is a 2D porous structure made of interconnected graphene sheets. The 2DG has a high surface area and high porosity, which makes it suitable for applications in catalysis, energy storage, and sensors. The 2DG was synthesized by a chemical method, and the PI was synthesized by a polymerization reaction. The 2DG and PI were then mixed and heated to form the 2DGP composite. The 2DGP composite has a porous structure and high thermal stability. The tensile strength and elongation at break of the 2DGP composite are 47.8 MPa and 2.7%, respectively, which are significantly higher than those of PI. The 2DGP composite also shows excellent electrical conductivity, with a volume resistivity of 32.3 Ω·cm and a surface resistivity of 2–18 Ω·cm. The 2DGP composite is suitable for applications in electronic devices and sensors.

*Corresponding author. E-mail address: liy@hust.edu.cn (Y. Li).

https://doi.org/10.1016/j.compositesa.2020.105904

Received 31 July 2020; Received in revised form 1 August 2020; Accepted 13 August 2020

Available online 18 April 2020

1359-835X/ © 2020 Elsevier Ltd. All rights reserved.

Ys. T. ... (SLM), ... (AM) ... (3D) ... *in-situ* ... SLM ... T ... Ys 20, ... Ys 21, ... Ni ... Ys 22. C ... / ... s ... C ... Ni ... CVD ... (< 0.001 %) ... Ys 23. W ... Ni ... (> 0.1 %) 17, ... 24. H ... SLM f ... Y ... s ... f ... (1000-1100). F ... s ... f ... SLM ... Y ... 25. T ... 3DG/ ... (3DG/C) ... SLM ... Y ... CVD ... A ... Y ... Y ... SLM f ...

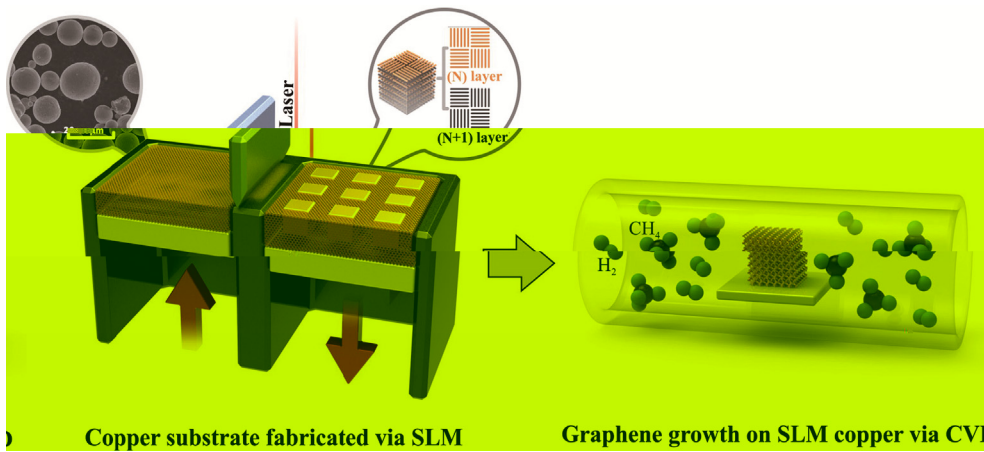


Fig. 1. In-situ fabrication of 3DG/C composites via SLM (left) and in-situ CVD (right). (For interpretation of the references to this figure caption, the reader is referred to the web version of this article.)

ASTMB193-2002 (2003) and ASTM E1461-2013 (2013) for mechanical testing. The tensile test was performed using a universal testing machine (LFA457, Instron) with a load cell of 5 kg. The test was conducted at room temperature (25 °C) with a crosshead speed of 0.5 mm/min. The test specimens were prepared according to the ASTM E1461-2013 standard. The tensile strength and elongation at break were recorded. The scanning electron microscope (SEM) was used to observe the surface morphology of the samples. The SEM was operated at 15 kV and 5 mm magnification. The SEM images were captured at 5000x magnification. The SEM images were processed using ImageJ software. The SEM images were used to analyze the surface morphology of the samples. The SEM images were used to analyze the surface morphology of the samples. The SEM images were used to analyze the surface morphology of the samples.

3. Results and discussion

3.1. Formation of SLM copper

3.1.1. SLM manufacturing of copper under different line energy densities

The SLM process was performed under different line energy densities. The line energy density was defined as the laser power divided by the scanning speed. The line energy densities were 100, 150, 200, 250, 300, 350, 400, 450, and 500 J/mm. The SLM process was performed under different line energy densities. The line energy density was defined as the laser power divided by the scanning speed. The line energy densities were 100, 150, 200, 250, 300, 350, 400, 450, and 500 J/mm. The SLM process was performed under different line energy densities. The line energy density was defined as the laser power divided by the scanning speed. The line energy densities were 100, 150, 200, 250, 300, 350, 400, 450, and 500 J/mm.

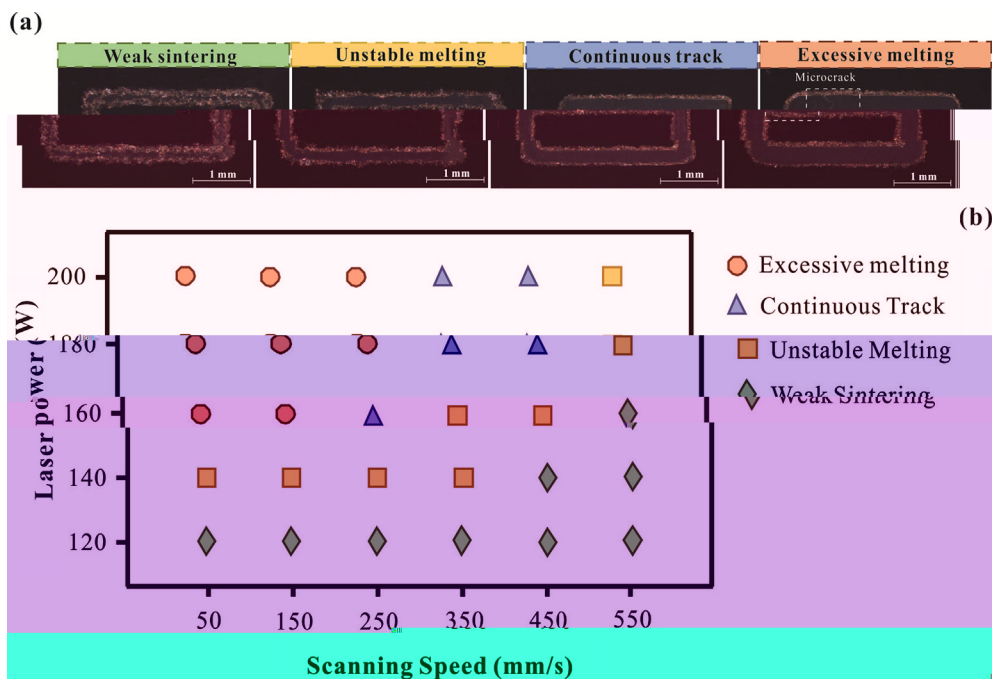


Fig. 2. (a) Typical SEM images of SLM copper tracks under different conditions: (A) Weak sintering, (B) Unstable melting, (C) Continuous track, and (D) Excessive melting. (b) Laser power vs Scanning Speed for different SLM conditions.

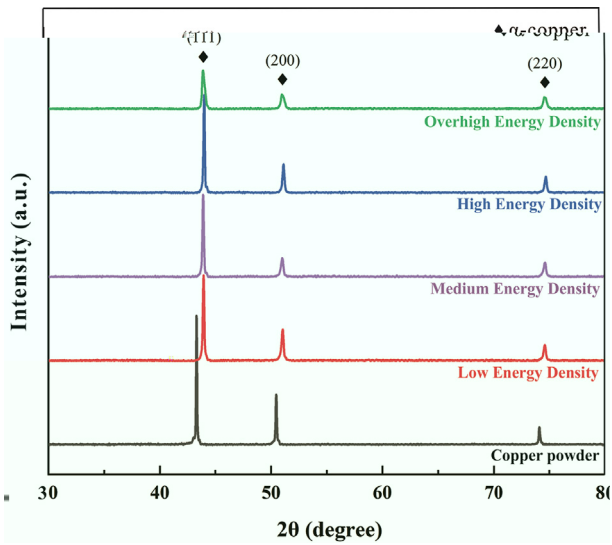


Fig. 3. XRD patterns of copper powder at different energy densities: (a) 3000 J/cm³, (b) 1800 J/cm³, (c) 857 J/cm³, (d) 285 J/cm³, (e) 128 J/cm³. The inset shows the magnified view of the (111) peak.

3.1.2. Formation of anisotropic microstructure under different volumetric energy density

The XRD patterns of copper powder at different energy densities are shown in Fig. 3. The (111) peak intensity is significantly higher than the (200) and (220) peaks, indicating a strong preferred orientation of the copper powder particles. The intensity of the (111) peak increases with increasing energy density, suggesting that higher energy density leads to a more pronounced anisotropic microstructure. The inset in Fig. 3 shows the magnified view of the (111) peak, which is fitted with a Lorentzian function to determine the peak position. The peak position of the (111) peak shifts slightly to a higher 2θ value as the energy density increases, indicating a change in the lattice spacing of the copper powder particles.

The XRD patterns of copper powder at different energy densities are shown in Fig. 3. The (111) peak intensity is significantly higher than the (200) and (220) peaks, indicating a strong preferred orientation of the copper powder particles. The intensity of the (111) peak increases with increasing energy density, suggesting that higher energy density leads to a more pronounced anisotropic microstructure. The inset in Fig. 3 shows the magnified view of the (111) peak, which is fitted with a Lorentzian function to determine the peak position. The peak position of the (111) peak shifts slightly to a higher 2θ value as the energy density increases, indicating a change in the lattice spacing of the copper powder particles.

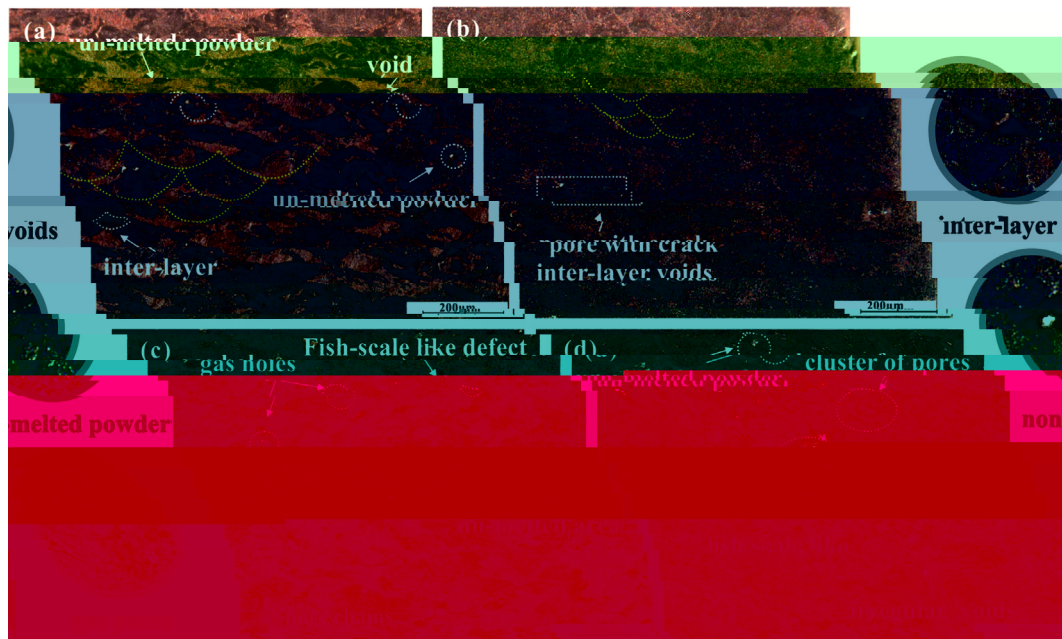


Fig. 4. SEM micrographs of SLM-processed copper powder at different energy densities: (a) 3000 J/cm³, (b) 1800 J/cm³, (c) 857 J/cm³, (d) 285 J/cm³. The inset shows the magnified view of the (111) peak.

... ..

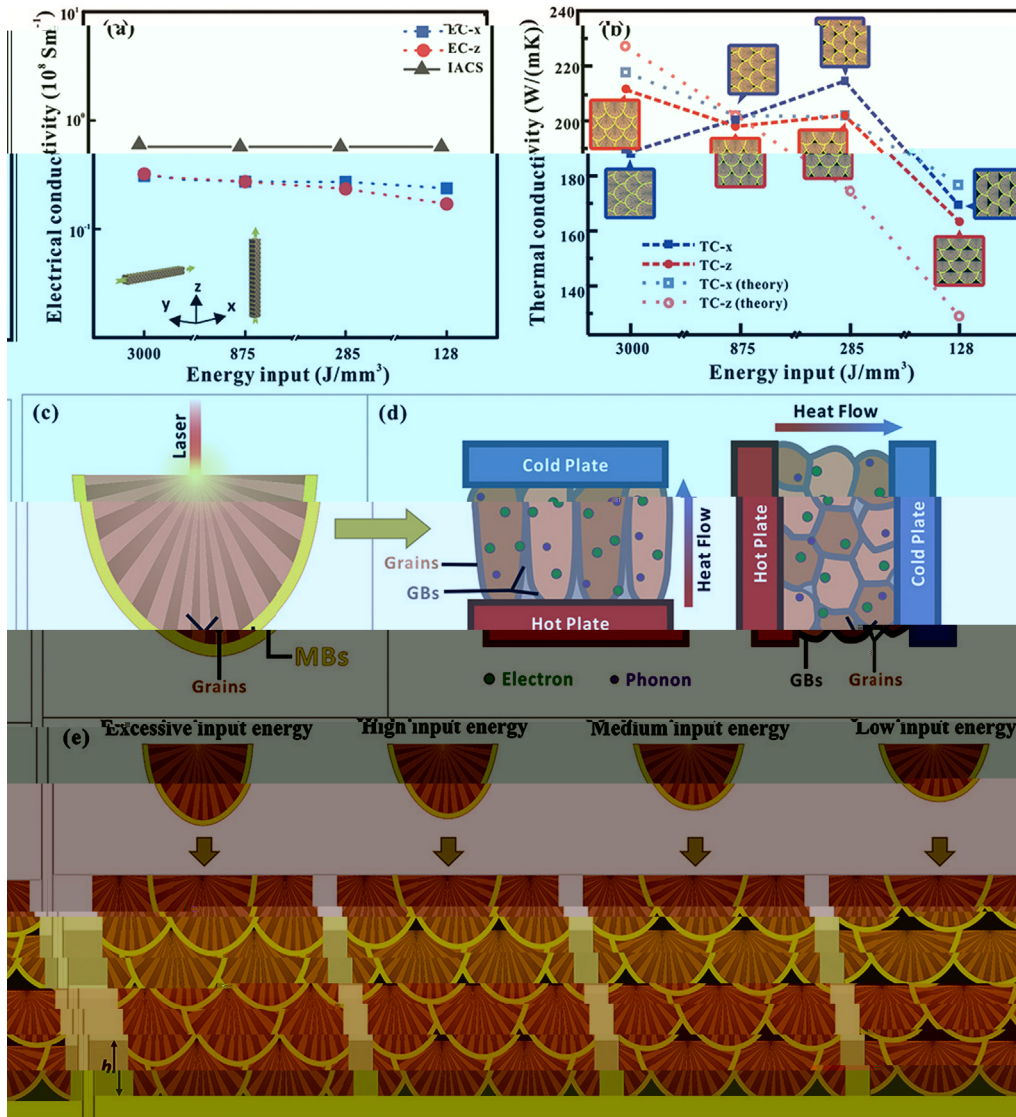


Fig. 7. (a) Electrical conductivity of 3DG/C porous scaffold as a function of energy input. (b) Thermal conductivity of 3DG/C porous scaffold as a function of energy input. (c) Schematic of the laser heating process. (d) Schematic of the thermal transport process. (e) Morphological evolution of 3DG/C porous scaffold under different energy inputs.

... is, ... y ... i ... f ... s ... si ... k ... s ...

3.3. Morphology and structure of CVD 3DG/Cu porous scaffolds

... El ... s ... s ... ff ... s ... d ... ff ... si ... y ...
 ... in-situ ... CVD ... As ...
 ... 39. A ... s ... y ...
 ... f 33 ... V ... C ... Ni, Li ... 40 ...
 ... 23 ... y ... f ... sf ... s ... 41 ...
 ... CVD ...

... A ... y ... i ... s ... i ... s ... f ... f ... f ...
 ... y ... s ... s ... si ... SEM, ... ss-s ...
 ... s ... f ... 3DG/C ... s ... s ... ff ...
 ... y 450 μm (Fig. 8a). A ... i ... fi ...
 ... y (Fig. 8b), ... fl ... s ...
 ... s ... f ... s ... ff ... s ... T ...
 ... EDS ...
 ... (Fig. 8c-d), ...
 ... 3DG/C ... y ...
 ... (Fig. 8e-g). T ... 3DG/C ...
 ... (Fig. 8h).
 ... R ... s ... y ... sf ... f ... 3DG/C ...
 ... 1590 ... G ... (~
 ... 2D- ... 2699 ...
 ... 42 (Fig. 8i). Si ...
 ... D- ... (~1350 ...)
 ... 43 ... si ... y ... f ... D ... G ... (I_D/I_G) ...

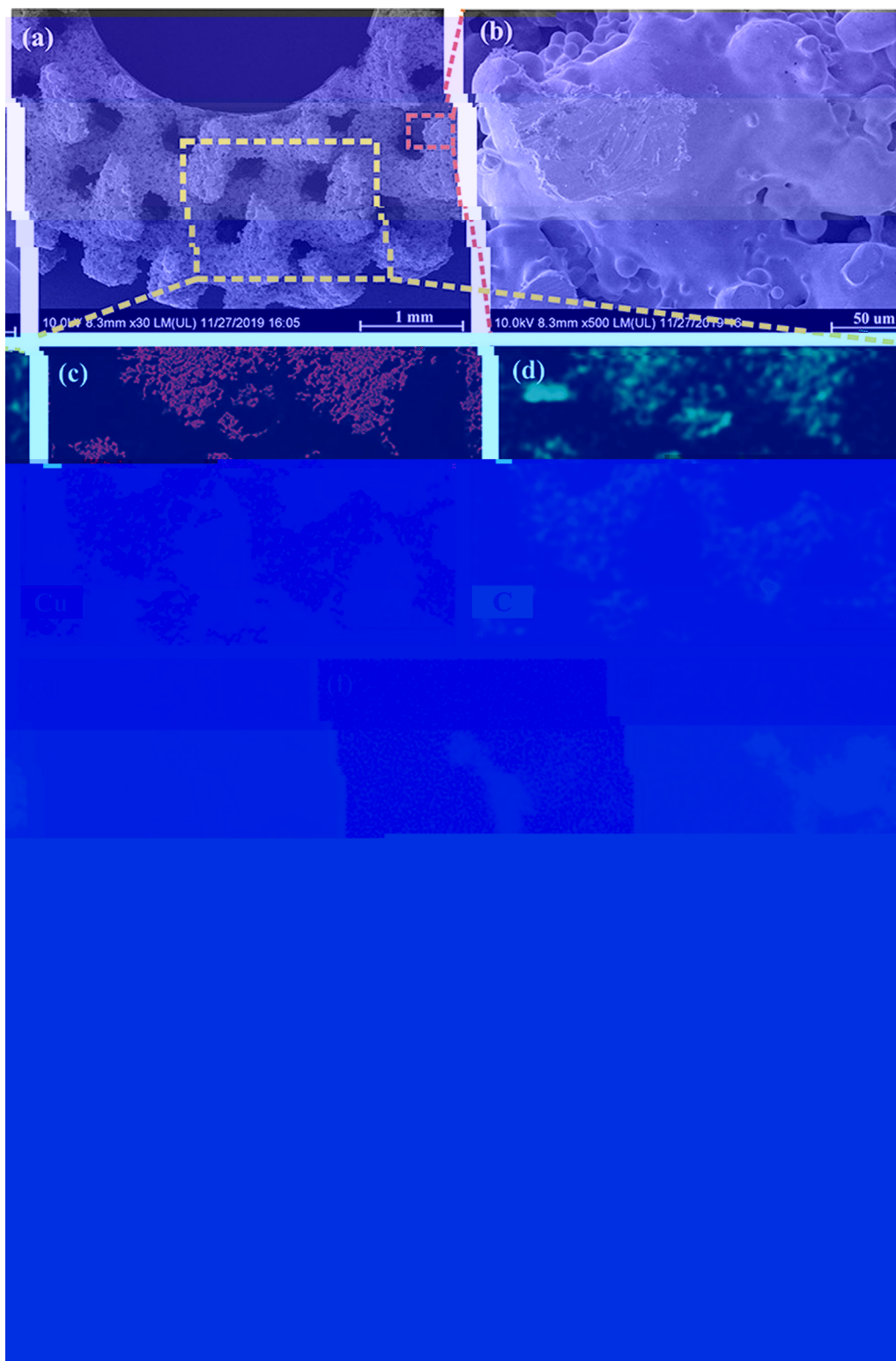


Fig. 8. (a) SEM image of 3DG/C porous scaffold; (b) High-magnification SEM image of 3DG/C porous scaffold; (c) EDS elemental map of 3DG/C porous scaffold; (d) EDS elemental map of 3DG/C porous scaffold. (f) C; (g) O; (h) Cu; (i) Zn; (j) Si; (k) Al; (l) Fe; (m) Ca; (n) Mg; (o) S; (p) P; (q) K; (r) Na; (s) Cl; (t) Br; (u) I; (v) F; (w) O; (x) N; (y) C.

...sily f...s. With s... fl...
 ...f I_D/I_G ... 0.71 0.93...
 ...As...
 ...f 1000 °C, fl... f CH₄... 30 s...
 20 (a) ...f 3DG/C...

3.4. Thermal property and EMI shielding effectiveness of 3DG/Cu porous scaffolds
 ...
 ... 26.8%...
 ... 14.8%...

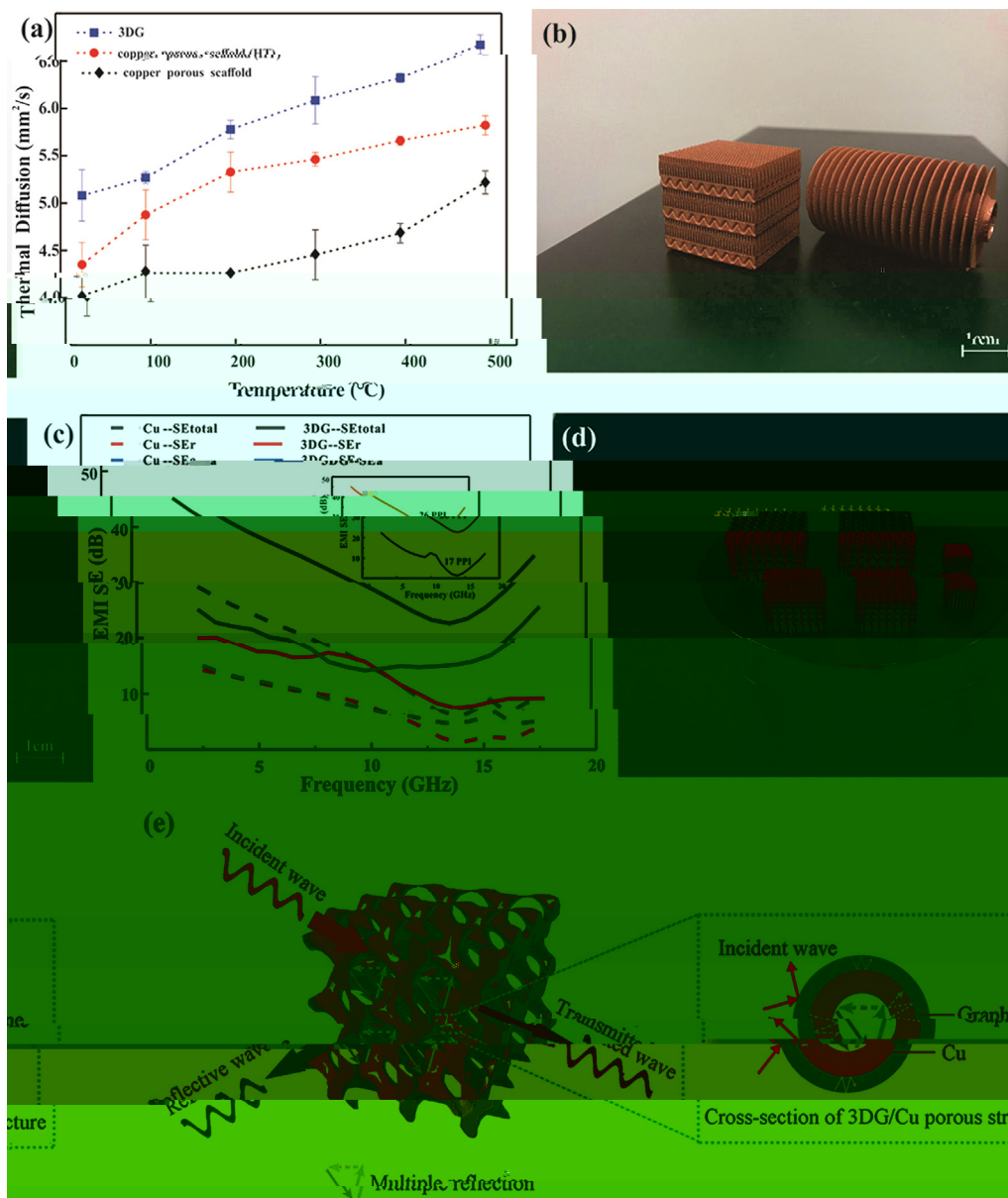


Fig. 9. Properties of 3DG/C porous scaffolds: (a) Thermal Diffusion; (b) SLM, (c) EMI SE; (d) SEM image of scaffold; (e) Schematic of wave interaction with the scaffold.

Table 1

Comparison of EMI shielding efficiency and improvement of thermal property for various composites.

Coating materials	Substrate	Method	Maximum shielding efficiency (dB)	Improvement of thermal property (%)	Ref
G	G	I	37	-	50
G	PS	H	29.3	-	56
G	PMMA	S	19	-	57
C/G	A	S	-	8.5	58
Ni	-	F	-	554	59
C-Ni	-	E	20	-	60
G	C	P	-	2.4	61
G	C	F	47	6.3	62
G	C	CVD + SLM	47.8	27	This work

Note: Y () Y ()-PPMA, Ys Y -PS.

Declaration of Competing Interest

The authors declare that they have no competing interests.

Acknowledgement

The authors thank the following individuals for their contributions: N. N. S. F. C. (N. 51671091, N. 51902295, N. 51675496). T. J. S. Y. F. R. S. F. S. C. U. S. C. U. S. F. G. S. (W.) (N. (N. CUG170677) H. P. N. S. F. (N. 2019 CFB264).

Appendix A. Supplementary data

Supplementary data is available at: //10.1016/j. 2020.105904.

References

- 1 BARG, N. N, M. S. YK, M. S. G. 2018;91:24-69.
- 2 BAA, G. S, B. W, C. L, T. D, M. F. 2008;8(3):902-7.
- 3 LI, H, C. S, M, P. H, P. O, S. G. 2016;8(36):24112-22.
- 4 KIM, K. J, J. B, C. K. JH, A. JH. G. 2017;11(8):7950-7.
- 5 P. C. M, H, M, T. M. L. D. P. 2020;262:118266-76.
- 6 LI, J. W, C. LL, J. SH, W. G. L. F. C-G. 2017;101:50-8.
- 7 HQ, L. SW, C. LH, J. SH, H. HQ. S. 2018;6(42):21216-24.
- 8 D. S. TM, S. P, D. S. Y. P, K. J, K. M, A. S. T. 3D. 2017;1(4):467-70.
- 9 Q. L, L. L, T. S. F. H. P. C. P. 2014;4(72):38273-80.
- 10 D. H. L. SP, N. W. JG. 3D. M. S. 2. P. A. 2016;90:424-32.
- 11 LI, L. W, S. CQ, H. MK, H. L, D. W. S. F. S. Y. 3D. EM. 201803938.
- 12 LI, J, P. S. O₂, C. R. G. N. S. D. G. ACSN. 2013;7(7):6001-6.
- 13 J. SH, A. S. G. A. L. S. Y. S. S. F. C. I. E. 2017;56:15520-38.
- 14 I. T. S. K. K. S. M. T. T. T. K. T. PCCP. 2018;20(9):6024-33.
- 15 S. K. D. N, M. C. V. S. J. N, E. J. T. Y. J. E. S. 2002;149(8):370-7.
- 16 C. H, S. M, S. WH, L. G, H. Q. P. 3D. S. 2017;7(22):3163-8.
- 17 K. S. H, G. M, J. S. L, H. J, W. C. C. M. U. M. 2019;1(4):1077-87.
- 18 S. Q. F. L, W, L, H, L. C. Y. A. M. 2017;29(31):1701583-90.
- 19 G. C. L, T. H. D, W. T. Y. ACSN. 2019. //10.1021/ 9.08191.
- 20 C. C. H. B. N, J, C. S, L, F. 3D. T:6A 4V. M. D. S. 2019;175:107824-33.
- 21 S. S. J, B. Z. C. D. T. F. N. B. S. Y. SLM. S. f. C. T. 2016;307:407-17.

- 22 R. DC, HB, L. J, Li, S, J, W. R. M. S. 2020;771:138586-95.
- 23 LI, C. W, A. J, K. S, N. J. D. L. S. S. 2009;324(5932):1312-4.
- 24 C. P, R. WC, G. LB, L. BL, P. SE, C. HM. T. S. Y. 2011;10:424-8.
- 25 J. SD, D. S, G. S. S. L, K. JP, H. JV, V. S. K. J. M. P. S. T. 2019;270:47-58.
- 26 W. H. L, L. T. D, C. Q, F. Eff. S. Y. M. D. S. 2019;170:107697-708.
- 27 G. DD, M. S. W, W. S. K, P. R. L. S. I. M. R. 2013;57(3):133-64.
- 28 LI, E, T. S. S, C. S. L, F. A. Eff. S. (SLM) S. J. M. P. S. T. 2017;249:255-63.
- 29 S. W. L, J, W. P, C. F. Y. S. f. T:6A 4V. A. P. Y. A: M. S. P. 2018;124:685-98.
- 30 LI, M. S, D. W, S. C. I. S. M. D. S. 2015;87:797-806.
- 31 L. CLA, M. S. S, T. M, A. RC, W. S. P, J, L. PD. T. ff. 2019;166:294-305.
- 32 T. K. T. WQ, T. J, D. S. S, M, M. D. R. T-6A-4V. S. IR. 2016;6:26039-48.
- 33 K. H, T. P, L. NH, T. SB, C. CK. G. Y. T-6A-4V. S. V. P. Y. 2016;11(3):183-91.
- 34 R. H. K, K. NV, G. H, S. TL, S. BE. M. S. J. M. E. P. f. 2013;22(12):3872-83.
- 35 T. K. T. J, V. S. G, P. Q, G. A. T-6A-4V. J. A. Y. C. 2015;646:303-9.
- 36 R. DA, M. LE, M. H. N. A. M. 2011;59(10):4088-99.
- 37 W. H. Eff. f. Y. S. C-2.4N-0.7S. Y. J. A. Y. C. 2018;743:258-61.
- 38 K. S. W. Y. S. E. I. 2003;23:309-48.
- 39 LI, G. S. J. ff. YR, G. S. N. P. E. C. (11). N. L. 2010;10(9):3512-6.
- 40 LI, S. C. WW, C. L. L. R. ff. R. Y. S. E. N. C. Y. S. N. L. 2009;9(12):4268-72.
- 41 W. C. W. H. SQ. L. A. S. 2020;161:479-85.
- 42 F. AC, M. Y. J, C, S. V. C. S. C. L. M. M. 1F. R. S. P. Y. R. L. 2006;97(18):187401-4.
- 43 S. G. J. SH, F. PC, H. HQ. F. Y. M. L. 2017;200:97-100.
- 44 J. K. H. J, C. J, D. F. C- Ni. Y. CNTs. A. S. f. S. 2014;311:351-6.
- 45 R. J. K, M. DP, A. S. C, M. S. S. j. K. E. EMI. S. 2018;12:475-84.
- 46 S. B, L. W. W. C. S. S. Y. f. S. (EMI) S. ACS. A. M. I. f. S. 2015;8(12):8050-7.
- 47 LI, N, H. D. F, H. L. G. 8.000.0.94979. J(L. 37T. (A.)-340.5400.0.9. 1.933.1. 73-342(1.04663956024445/CS005)T342.6 D. S.)-2

M 2019;34(5):489–98.

53 W B, C M, L M. R. ... s. A M 2014;26:3484–9.

54 C H, W S, J J, C J, SY ... f F₃O₄ ... Y(Y) ... s P A 2019;121:139–48.

55 W L, J, Q. T. ff, f MWCNTs ... s. J M S. M E 2015;26(3):1895–9.

56 D P, GR, H P, Q F, M B, ML. Effi ... s. J M C 2012;22:18772–4.

57 HB, Q, WG, H, T ... y ... ACSA M I f, s 2011;3:918–24.

58 S A, U, N, T, V. T. ... f M f, R 2016. s:// /10.1051/ f /2016021.

59 P s MT, J, H, R ff RS, S L. T. ... s ff - y ... N L 2012;12:2959–64.

60 J, K, H, H, D, P f ... f C-Ni, y ... M L 2017;122:244–7.

61 R H, L S, B S, K TW, L DS, L HJ, T ... s f ... S, R 2015. s:// /10.1038/s 12710.

62 T, F SG, Li, G Q, Li, G, R KP, SY ... y y ... s s Y, s 3D, s/ y y ... M S, E A-S 2020. s:// /10.1016/j. s. 2019.105670.

63 R DA, M LE, M E, H DH, M JL, M BI, N ... s ... A M 2011;59(10):4088–99.

64 E s SF, Li, KC, S, VK, M IC. T ... y s f, J T s 1973;1(1):10–38.